

EXPRESS LETTER

# Visualizing the Local Twist Angle Variation within and between Domains of Twisted Bilayer Graphene

To cite this article: Jiawei Hu *et al* 2024 *Chinese Phys. Lett.* **41** 037401

View the [article online](#) for updates and enhancements.

## You may also like

- [Advanced atomic force microscopies and their applications in two-dimensional materials: a review](#)  
Rui Xu, Jianfeng Guo, Shuo Mi et al.
- [Local characterization of mobile charge carriers by two electrical AFM modes: multi-harmonic EFM versus sMIM](#)  
Le Lei, Rui Xu, Shili Ye et al.
- [Moiré phonons in twisted MoSe<sub>2</sub>-WSe<sub>2</sub> heterobilayers and their correlation with interlayer excitons](#)  
Philipp Parzefall, Johannes Holler, Marten Scheuck et al.

## Visualizing the Local Twist Angle Variation within and between Domains of Twisted Bilayer Graphene

Jiawei Hu(户佳玮)<sup>1,2†</sup>, Shiyu Zhu(朱诗雨)<sup>1,2\*†</sup>, Qianying Hu(胡倩颖)<sup>1,2†</sup>, Yunhao Wang(王云昊)<sup>1,2</sup>,  
Chengmin Shen(申承民)<sup>1,2</sup>, Haitao Yang(杨海涛)<sup>1,2</sup>, Xiaoshan Zhu(竺晓山)<sup>1,2</sup>,  
Qing Huan(郇庆)<sup>1,2</sup>, Yang Xu(许杨)<sup>1,2\*</sup>, and Hong-Jun Gao(高鸿钧)<sup>1,2,3\*</sup>

<sup>1</sup>Beijing National Center for Condensed Matter Physics, and Institute of Physics,  
Chinese Academy of Sciences, Beijing 100190, China

<sup>2</sup>School of Physical Sciences, University of Chinese Academy of Sciences, Beijing 100190, China

<sup>3</sup>Hefei National Laboratory, Hefei 230088, China

(Received 26 February 2024; accepted manuscript online 4 March 2024)

Moiré superlattices in twisted two-dimensional materials have emerged as ideal platforms for engineering quantum phenomena, which are highly sensitive to twist angles, including both the global value and the spatial inhomogeneity. However, only a few methods provide spatial-resolved information for characterizing local twist angle distribution. Here we directly visualize the variations of local twist angles and angle-dependent evolutions of the quantum states in twisted bilayer graphene by scanning microwave impedance microscopy (sMIM). Spatially resolved sMIM measurements reveal a pronounced alteration in the local twist angle, approximately  $0.3^\circ$  over several micrometers in some cases. The variation occurs not only when crossing domain boundaries but also occasionally within individual domains. Additionally, the full-filling density of the flat band experiences a change of over  $2 \times 10^{11} \text{ cm}^{-2}$  when crossing domain boundaries, aligning consistently with the twist angle inhomogeneity. Moreover, the correlated Chern insulators undergo variations in accordance with the twist angle, gradually weakening and eventually disappearing as the deviation from the magic angle increases. Our findings signify the crucial role of twist angles in shaping the distribution and existence of quantum states, establishing a foundational cornerstone for advancing the study of twisted two-dimensional materials.

DOI: 10.1088/0256-307X/41/3/037401

Two-dimensional moiré materials have attracted much attention for the novel quantum phases with strong electronic correlations and their wide tunability of the moiré wavelength, symmetry, and band topology.<sup>[1]</sup> The twist angle and electronic states under long-wavelength periodic potentials lead to the emergence of flat bands and various interaction-driven phenomena including correlated insulators, superconductivity, and integer/fractional quantum anomalous Hall effect.<sup>[2–7]</sup> In twisted homobilayers, specifically, small variations in twist angles can strongly affect the stability of multiple competing orders and cause dramatically different ground states, enriching the phase diagram and resulting in sensitive relationships between the structural details of stacked layers and the correlated phenomena.<sup>[8,9]</sup>

It has been found experimentally that the local twist angle can vary substantially in the same sample caused by random strain fluctuations.<sup>[10–18]</sup> Such inhomogeneities of twisted two-dimensional devices can easily hinder the global measurements of novel quantum states in mesoscopic samples and compromise the ability to align experimental measurements with predictive theoretical models.<sup>[14,19–24]</sup> The missing information about local twist angle distribution and correlated electronic states presents a critical roadblock toward further understanding in this field.<sup>[25]</sup>

In this Letter, we directly visualize the spatially re-

solved conductivity and local twist angles in a twisted bilayer graphene (TBG) device through scanning microwave impedance microscopy (sMIM) measurements. By varying the magnetic field and back-gate voltage, the moiré band gaps, quantum Hall states (QHSs), and Chern insulators (ChIs) are identified in sMIM point measurements.<sup>[26–29]</sup> The spatial mapping of local twist angles is obtained from the doping density of moiré band gaps in sMIM linecuts and images. Significant variations in local twist angles are evident in this device, particularly when crossing domain boundaries, and at times, variability is observed even within individual domains. The ChIs display a pronounced dependence on the local twist angles. They gradually weaken and ultimately vanish as deviating from the magic angle ( $1.1^\circ$ ). Our experiments figure out the local twist angle variation between and within domains, as well as the angle-dependent evolutions of corresponding quantum states, providing a pathway for the simultaneous measurements of local twist angle and quantum states.

We fabricated our TBG sample using the dry transfer and ‘tear-and-stack’ technique<sup>[30,31]</sup> and deposited the hBN/TBG/hBN (hexagonal boron nitride) stack onto a SiO<sub>2</sub>/Si substrate [Fig. 1(a)]. The sample is targeted at a global twist angle near the magic angle ( $1.1^\circ$ ) between two graphene layers, but inevitably exhibits some local twist angle disorders. The layer-stacking structure and local conductivity are characterized by sMIM measure-

<sup>†</sup>These authors contributed equally to this work.

\*Corresponding authors. Email: syzhu@iphy.ac.cn; yang.xu@iphy.ac.cn; hjgao@iphy.ac.cn

© 2024 Chinese Physical Society and IOP Publishing Ltd

ments under low-temperature ( $T = 100$  mK) and vector magnetic field ( $9_z-3_x-1_y$  T). The microwave signals are obtained using non-contact sMIM scanning with constant height mode. The sMIM conductance image and spectra shown in the figures are all taken from the imaginary chan-

nel (sMIM-Im) where the intensity increases monotonically with the local conductivity.<sup>[32]</sup> Consequently, the distribution of local conductivity in TBG devices is distinctly observed through sMIM-Im mappings.<sup>[33–35]</sup>

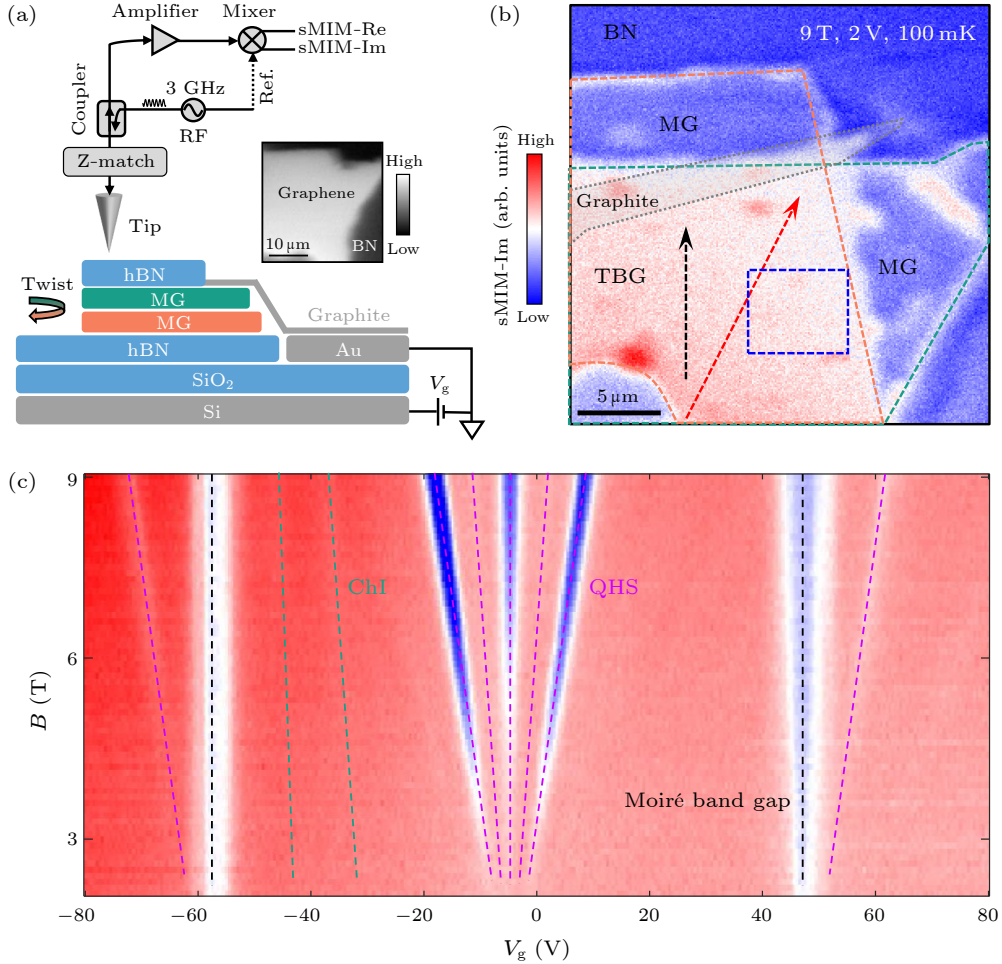


**Fig. 1.** Structure and quantum states of TBG measured by sMIM. (a) Schematic of the sMIM experimental setup and TBG device structure.  $V_g$  is the gate voltage. Inset: AFM image of the TBG device. (b) Large area sMIM-Im mapping of TBG device at  $B = 9$  T,  $V_g = 2$  V, and  $T = 100$  mK, showing the regions of monolayer graphene (MG) and TBG. (c) The sMIM point measurement at the location of TBG region, with the  $B$  sweeping from 2 T to 9 T, and the  $V_g$  sweeping from  $-80$  V to 80 V. Various kinds of electronic states including the ChI, QHS, and moiré band gaps are observed.

In our device, the regions of MG and TBG are distinguishable in the sMIM image under the magnetic field of 9 T and the gate voltage of 2 V [Fig. 1(b)]. The striking contrast between MG and TBG arises from distinct Landau level filling conditions. The MG regions show integer filling of Landau levels and leave the Fermi level in the gap, resulting in the insulating bulk states accompanied by quantum Hall edge states. In contrast, the TBG region shows incomplete filling of Landau level and overall high conductivity.

To investigate the electronic characteristics in TBG, we performed sMIM point measurements at fixed locations, depicting the sMIM-Im intensity as a function of the out-of-plane magnetic field ( $B$ ) and gate voltage ( $V_g$ ). Such a point measurement [Fig. 1(c)] reveals various quan-

tum states including QHS, ChI, and the moiré band gaps. These states are characterized by the intercept ( $s$ ) and slope ( $t$ ) of the evolution of insulating states, where  $s$  is the moiré filling factor, and  $t$  is Chern number as well as the flux filling factor.<sup>[36]</sup> Further, complete information on local electronic properties is obtained, including the local charge neutrality point (CNP), the gate capacitance ( $C_g$ ), and twist angles ( $\theta$ ).

In a TBG Landau fan diagram, the voltage of QHSs vary linearly with magnetic field  $B$ , with the carrier density ( $n$ ) following  $n = tB/\phi_0$ , where the magnetic flux quantum  $\phi_0 = h/e$  ( $e$  is the elementary charge,  $h$  is Planck's constant). The carrier density is experimentally modulated by the gate voltage as the function of  $n = C_g V_g$ . Derived from the QHSs in Landau fans within MG and

bilayer-graphene (BG) regions, the gate capacitance is approximately  $1.0255 e^{-8} F/cm^2$ .

We characterize the inhomogeneity of the local twist angle and corresponding quantum states by performing sMIM linecut measurements (local conductivity varies as a function of spatial positions and gate voltages) at 9 T in the TBG region. One of the linecut [Fig. 2(a)] shows the twist angle evolution when scanning along the black ar-

row as marked in Fig. 1(b). Three domains are discernible along the line, identified by the voltage value jump of the moiré full-filling gaps (four electrons filling in per moiré supercell) at  $V_{ns}$  and  $V_{-ns}$ . Additionally, the corresponding shifted Landau levels with  $s = \pm 4$  [purple dashed lines in Fig. 2(a)] further emphasize the presence of varying twist angles  $\theta$ .

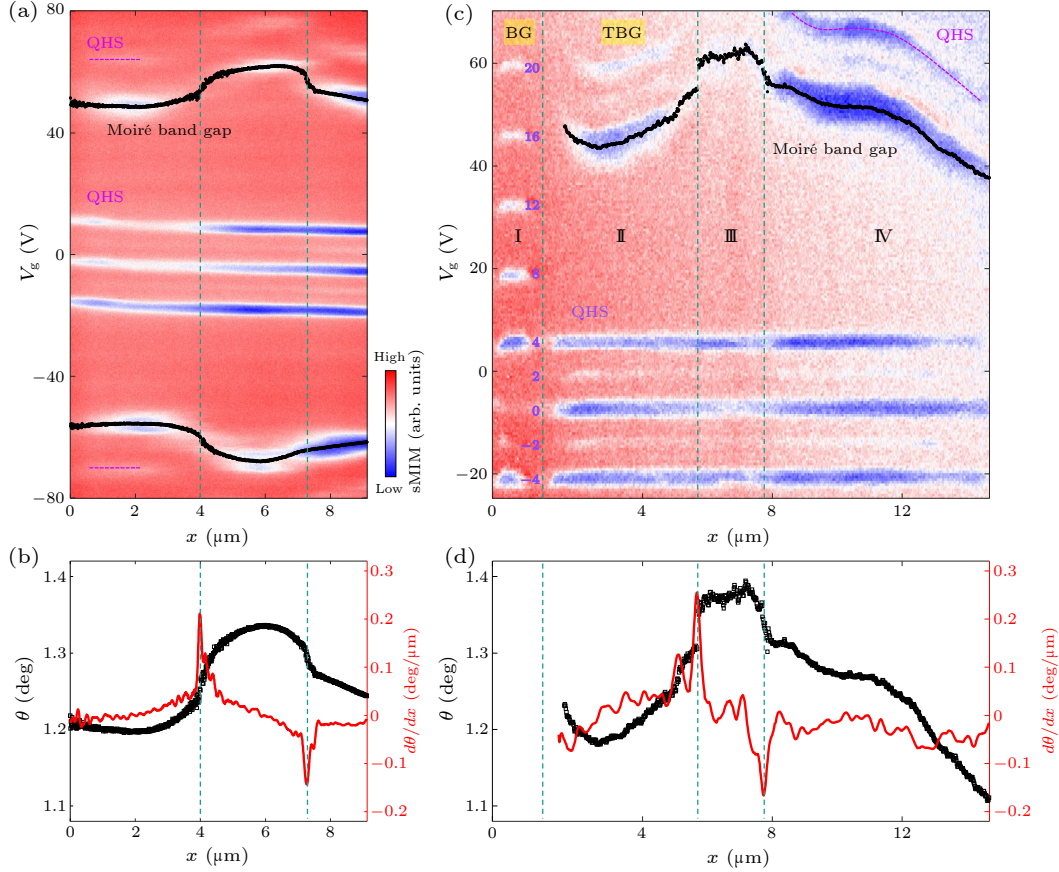


**Fig. 2.** Variation of local twist angle and quantum states within and between domains. (a) An sMIM linecut with  $B = 9$  T and  $V_g$  sweeping from  $-80$  V to  $80$  V, extending over  $9 \mu\text{m}$  along the black arrow marked in Fig. 1(b). The centers of moiré band gaps are marked by black dots. Three domains with distinct  $V_g$  values for moiré band gaps are observed. (b) Local twist angle variation  $\theta$  (black squares) and its derivative  $d\theta/dx$  (red line) along the linecut, as shown in (a). Peak and dip are observed in  $d\theta/dx$  at the location of domain boundaries. (c) Another sMIM linecut with  $B = 9$  T and  $V_g$  sweeping from  $-25$  V to  $70$  V, extending over  $15 \mu\text{m}$  along the red arrow marked in Fig. 1(b). The centers of moiré band gaps are marked by black dots. Four domains, including both BG and TBG regions, have been identified. (d) Local twist angle variation  $\theta$  (black squares) and its differential  $d\theta/dx$  (red line) along the linecut, as shown in (c). Peak and dip are observed in  $d\theta/dx$  at the location of domain boundaries.

By fitting a series of  $V_g$ -sweeping spectra at different locations, we figure out the variation of twist angles [black squares in Fig. 2(b)]. The diverse voltage values of moiré band gaps originate from the varying local twist angles. This correlation is governed by the formula  $\sin \theta = a \sqrt{C_g \Delta V_g} \sqrt{3}/16$ , where  $a = 0.246$  nm is the graphene lattice constant and  $\Delta V_g = V_{ns} - V_{-ns}$  is the difference between gate voltages of moiré band gaps on electron and hole doped sides. The obtained local twist angles exhibit variation of about  $0.14^\circ$ , ranging from  $\theta = 1.20^\circ$  to  $\theta = 1.34^\circ$  across the  $9 \mu\text{m}$  pathway. The  $d\theta/dx$  profile exhibits clear peaks and dips at the domain boundaries [red line in Fig. 2(b)], effectively partitioning the twist an-

gles into three sections with values near  $1.20^\circ$ ,  $1.33^\circ$ , and  $1.26^\circ$ . Remarkably, the QHSs maintain continuity even when undergoing the twist angle variation across different domains.

In contrast to discrete domains of twist angles, an alternative linecut [Fig. 2(c)] presents more intricate variations in local twist angles, spanning a broader range of about  $0.28^\circ$  [Fig. 2(d)], ranging from  $\theta = 1.11^\circ$  to  $\theta = 1.39^\circ$  over the  $15 \mu\text{m}$  pathway along the red arrow as marked in Fig. 1(b). Based on variations in quantum states and twist angles, four distinct sections are discerned.

For  $x < 2 \mu\text{m}$  (section I), distinct characteristics of Bernal BG with a relaxed twist angle ( $\theta = 0^\circ$ ) are ob-

served, displaying QHS with the filling factors ranging from  $t = 0, \pm 2, \pm 4$  to as high as  $t = 20$ . The quantum states in BG present a notable contrast with those in TBG sections, resulting in a sudden disappearance of moiré bands gaps. The domain boundaries among sections II–IV are indicated by peaks and dips in the  $d\theta/dx$  profile, wherein section III exhibits relatively uniform twist angles with a value of  $\theta$  near  $1.38^\circ$ . However, twist angles in sections II and IV vary continuously, suggesting the presence of twist angle disorder and local strains within

certain domains.

In addition to measurements performed under finite magnetic fields, the identification of local twist angles and quantum states can also be carried out under zero-field conditions. In such cases, only moiré band gaps remain pronounced in the spectra, while QHSs are naturally absent. To generate a direct visualization of the local twist angle  $\theta(\mathbf{r})$  and the charge variation  $\delta n(\mathbf{r})$ , we perform  $V_g$ -dependent sMIM measurements in an area of  $6 \mu\text{m} \times 5 \mu\text{m}$  as marked by a blue dashed box in Fig. 1(b).

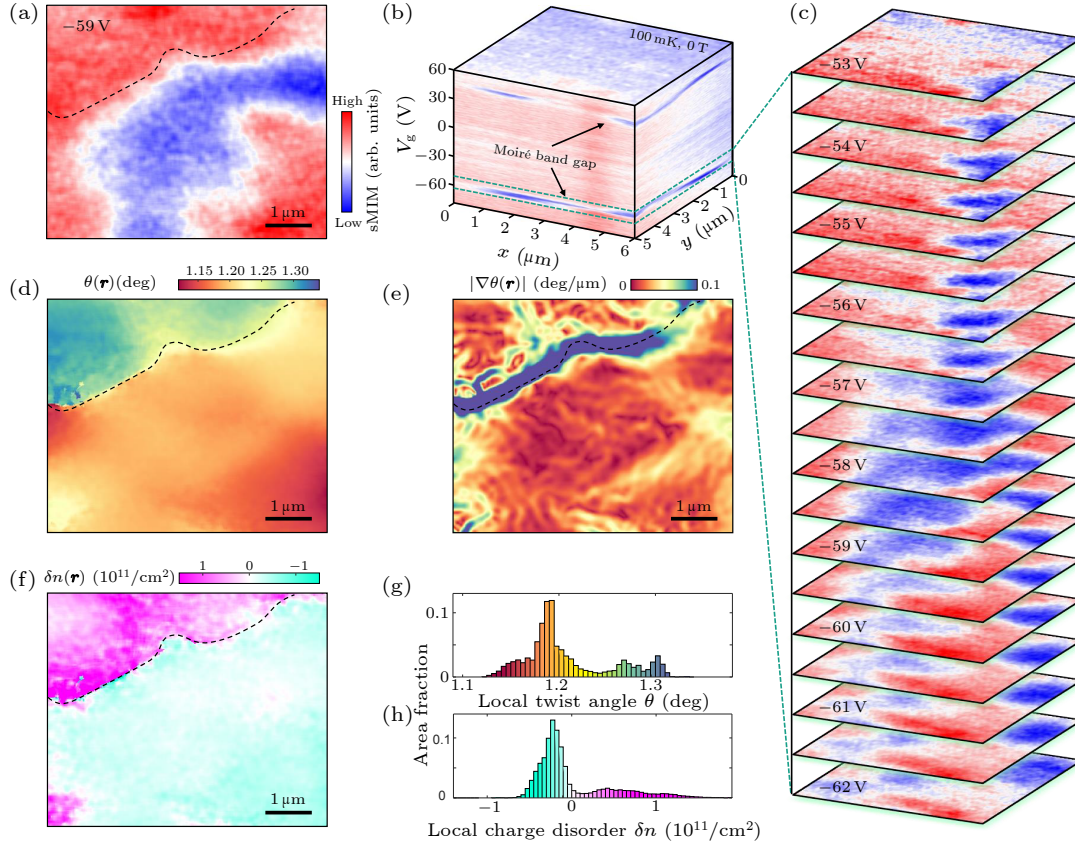


**Fig. 3.** Images of local twist angle and charge variation in a TBG area at zero field. (a) An sMIM-Im image of a TBG area ( $6 \mu\text{m} \times 5 \mu\text{m}$ ), marked by blue dashed box in Fig. 1(b), at  $B = 0 \text{ T}$ ,  $V_g = -59 \text{ V}$  and  $T = 100 \text{ mK}$ . (b) A 3D view of the conductivity tomography plot over the same area as (a), with  $V_g$  sweeping from  $-80 \text{ V}$  to  $60 \text{ V}$ . (c) A series of sMIM tomography slices (b) with different  $V_g$  ranging from  $-53 \text{ V}$  to  $-62 \text{ V}$ . The blue blocks signify locations with poor conductivity within moiré band gaps. (d)–(e) Images of the twist angle  $\theta(\mathbf{r})$  (d) and its gradient  $|\nabla\theta(\mathbf{r})|$  (e) obtained from sMIM tomography in (b). (f) Image of the charge variation  $\delta n(\mathbf{r})$  obtained from sMIM tomography in (b). The values are determined by  $V_g$  of the insulating state at moiré band gaps. (g)–(h) Histograms of the twist angle  $\theta$  (g) and charge variation  $\delta n$  (h) as depicted in (d) and (f). The histograms reveal the bimodal distribution characteristics in the numerical values, consistent with the observation of two domains within this area.

The presence of local electronic inhomogeneity becomes readily apparent through a single sMIM image showing the local conductivity with gate voltage  $V_g = -59 \text{ V}$  [Fig. 3(a)]. A comprehensive representation of insulating states in this region is contained in a slice of the three-dimensional (3D) conductivity tomographic plot [Fig. 3(b)], illustrating the evolution of two moiré band gaps with sweeping gate voltages from  $-80 \text{ V}$  to  $60 \text{ V}$ . The moiré band gaps manifest as insulating stripes at the tomography side surface. A series of sMIM tomography slices with  $V_g$  ranging from  $-53 \text{ V}$  to  $-62 \text{ V}$ , provides a more detailed and intuitive depiction of this evolution.

The blue blocks delineate the locations of moiré band insulator regions, while the white and red blocks represent areas with higher conductivity. As gate voltage varies, the moiré band insulator regions flow and change, pointing to variations in local twist angles.

We derive the distribution of the local twist angles  $\theta(\mathbf{r})$  [Fig. 3(d)] by processing the data through map smoothing and moiré band gaps fitting in each spectrum. Linear interpolation is also employed for specific individual pixels with incomplete information on moiré band gaps. As revealed by the  $\theta(\mathbf{r})$  image, the area is evidently distinguished into two domains, with the boundary marked by

dashed lines. The red/orange domain holds the twist angles concentrated within the range between  $1.15^\circ$  and  $1.20^\circ$  and the blue/green domain holds those between  $1.25^\circ$  and  $1.30^\circ$ . The domain boundary is manifested as a yellow stripe in the  $\theta(\mathbf{r})$  image and stands out as a clear ridge in the gradients  $|\nabla\theta(\mathbf{r})|$  [Fig. 3(e)]. Remarkably, even within single domains, the local twist angles show slight variations, which is in good agreement with the finding in the sMIM linecut [Figs. 2(c)–2(d)].

Additionally, the local charge variation  $\delta n(\mathbf{r})$  is another crucial electronic characteristic that leads to shifts in all quantum states in the direction of  $V_g$ . The distribution of  $\delta n(\mathbf{r})$  is derived through variations in the CNP, following the formula  $n(\mathbf{r}) = C_g V_{\text{CNP}}(\mathbf{r}) = C_g (V_{\text{ns}} + V_{-\text{ns}})/2$  and  $\delta n(\mathbf{r}) = n(\mathbf{r}) - \bar{n}$ . The local charge variation shows

a step change at the domain boundary and remains relatively uniform in each domain. The histograms reveal a bimodal distribution of local twist angles and local charge, consistent with the observation in  $\theta(\mathbf{r})$ ,  $|\nabla\theta(\mathbf{r})|$ , and  $\delta n(\mathbf{r})$  maps.

These variations in twist angles act as sensitive indicators, offering a glimpse into the nuanced interplay both between and within TBG domains. Additionally, Figs. 3(d)–3(f) correspond to the relaxation of strain and stress distributions, emphasizing the intricate relationship that underscores the material's response to mechanical forces. This detailed examination unveils the material's dynamic behavior in the face of external forces, contributing to a deeper understanding of its mechanical properties and potential applications in advanced material engineering.

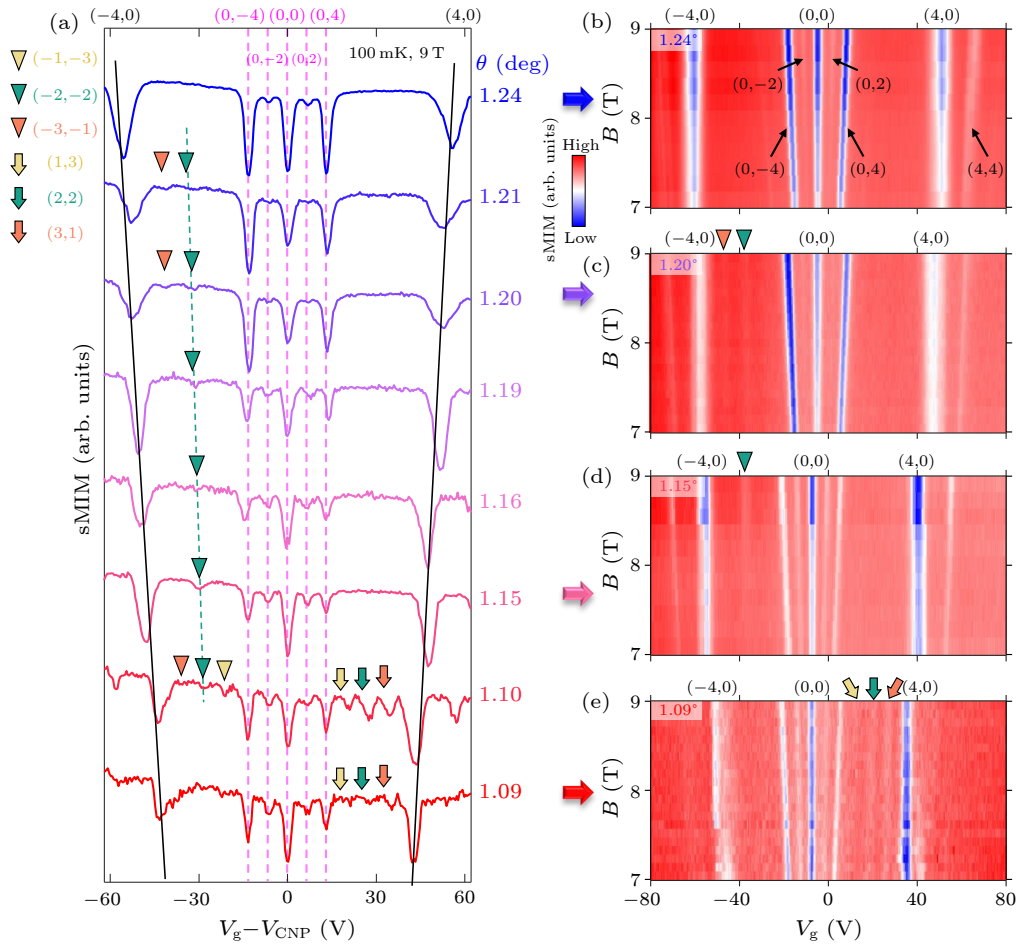


**Fig. 4.** Local twist angle dependence of correlated Chern insulator states in TBG. (a) Twist angle dependent sMIM spectra measured in TBG regions with  $B = 9$  T and  $T = 100$  mK. The quantum numbers of emergent Chern insulators are denoted by  $(s, t)$ , where  $s$  is the moiré filling factor and  $t$  is Chern number. (b)–(e) Several sMIM point measurements with the local twist angle of  $1.24^\circ$  (b),  $1.20^\circ$  (c),  $1.15^\circ$  (d), and  $1.09^\circ$  (e). Chern insulators are present in (c)–(e) while absent in (b).

In addition to shifting the QHSs and moiré band gaps, twist angle disorders also modulate the existence of quantum states, such as the ChIs. We present several sMIM spectra measured at positions with twist angles varying from  $1.09^\circ$  to  $1.24^\circ$  [Fig. 4(a)] and denote the ChIs by color-coding symbols.<sup>[37]</sup> The characteristics of different types of quantum states are identified in point measure-

ments [Figs. 4(b)–4(e)].

Besides the evident moiré bands gap and QHSs throughout these spectra, ChIs with a non-zero slope ( $t \neq 0$ ) and non-zero intercept ( $s \neq 0$ ) are also observed in the proximity of the magic angle ( $1.1^\circ$ ). Examining individual spectra, the ChIs exhibits a synchronized shift with moiré band gaps, gradually weakening as the local twist

angle deviates from the magic angle. Notably, as the deviation progresses, reaching  $1.24^\circ$ , the ChIs vanish entirely. These observations quantify the influence of local twist angles on the emergence of correlated ChIs, thereby providing insights into the systematic angle-dependent phase diagram of TBG.

In summary, we directly visualize the spatial distribution of the local twist angle between and within domains, and reveal its influence on the evolutions of correlated Chern insulators in TBG through sMIM measurements. The ChIs vanish in specific regions when the twist angle exceeds  $1.24^\circ$ , significantly deviating from the magic angle value of  $1.1^\circ$ . The variation introduces significant inhomogeneity in the device, elucidating the reasons behind the instability and disappearance of quantum states in certain ‘tear-and-stack’ devices. Our results pave the way for local twist angle detection and emphasize the critical role of twist angle distribution in shaping quantum states, laying a solid groundwork for advancing the exploration of twisted two-dimensional materials.

*Acknowledgments.* This work was supported by the National Natural Science Foundation of China (Grant Nos. 61888102 and 12374199), the National Key Research & Development Projects of China (Grant Nos. 2022YFA1204100, 2019YFA0308501, and 2021YFA1401300), the Chinese Academy of Sciences (Grant No. XDB33030100), and the Innovation Program of Quantum Science and Technology (Grant No. 2021ZD0302700).

## References

- [1] Kennes D M, Claassen M, Xian L, Georges A, Millis A J, Hone J, Dean C R, Basov D N, Pasupathy A N, and Rubio A 2021 *Nat. Phys.* **17** 155
- [2] Balents L, Dean C R, Efetov D K, and Young A F 2020 *Nat. Phys.* **16** 725
- [3] Mak K F, and Shan J 2022 *Nat. Nanotechnol.* **17** 686
- [4] Park H, Cai J Q, Anderson E, Zhang Y N, Zhu J Y, Liu X Y, Wang C, Holtzmann W, Hu C, Liu Z, Taniguchi T, Watanabe K, Chu J H, Cao T, Fu L, Yao W, Chang C Z, Cobden D, Xiao D, and Xu X D 2023 *Nature* **622** 74
- [5] Xu F, Sun Z, Jia T T, Liu C, Xu C, Li C S, Gu Y, Watanabe K, Taniguchi T, Tong B, Jia J, Shi Z W, Jiang S, Zhang Y, Liu X, and Li T X 2023 *Phys. Rev. X* **13** 031037
- [6] Li X F, Sun R X, Wang S Y, Li X, Liu Z B, and Tian J G 2022 *Chin. Phys. Lett.* **39** 037301
- [7] Ma J J, Wang Z Y, Xu S G, Gao Y X, Zhang Y Y, Dai Q, Lin X, Du S X, Ren J, and Gao H J 2022 *Chin. Phys. Lett.* **39** 047403
- [8] Bistrizter R, and MacDonald A H 2011 *Proc. Natl. Acad. Sci. USA* **108** 12233
- [9] Cao Y, Rodan-Legrain D, Park J M, Yuan N F Q, Watanabe K, Taniguchi T, Fernandes R M, Fu L, and Jarillo-Herrero P 2021 *Science* **372** 264
- [10] Li G H, Luican A, Lopes dos Santos J M B, Castro Neto A H, Reina A, Kong J, and Andrei E Y 2010 *Nat. Phys.* **6** 109
- [11] Kerelsky A, McGilly L J, Kennes D M, Xian L, Yankowitz M, Chen S, Watanabe K, Taniguchi T, Hone J, Dean C, Rubio A, and Pasupathy A N 2019 *Nature* **572** 95
- [12] Xie Y L, Lian B, Jäck B, Liu X M, Chiu C L, Watanabe K, Taniguchi T, Bernevig B A, and Yazdani A 2019 *Nature* **572** 101
- [13] Butz B, Dolle C, Niekil F, Weber K, Waldmann D, Weber H B, Meyer B, and Spiecker E 2014 *Nature* **505** 533
- [14] Uri A, Grover S, Cao Y, Crosse J A, Bagani K, Rodan-Legrain D, Myasoedov Y, Watanabe K, Taniguchi T, Moon P, Koshino M, Jarillo-Herrero P, and Zeldov E 2020 *Nature* **581** 47
- [15] Grover S, Bocarsly M, Uri A, Stepanov P, Di Battista G, Roy I, Xiao J W, Meltzer A Y, Myasoedov Y, Pareek K, Watanabe K, Taniguchi T, Yan B, Stern A, Berg E, Efetov D K, and Zeldov E 2022 *Nat. Phys.* **18** 885
- [16] Choi Y, Kim H, Peng Y, Thomson A, Lewandowski C, Polski R, Zhang Y, Arora H S, Watanabe K, Taniguchi T, Alicea J, and Nadj-Perge S 2021 *Nature* **589** 536
- [17] Turkel S, Swann J, Zhu Z Y, Christos M, Watanabe K, Taniguchi T, Sachdev S, Scheurer M S, Kaxiras E, Dean C R, and Pasupathy A N 2022 *Science* **376** 193
- [18] Yoo H, Engelke R, Carr S, Fang S, Zhang K, Cazeaux P, Sung S H, Hovden R, Tsen A W, Taniguchi T, Watanabe K, Yi G C, Kim M, Luskin M, Tadmor E B, Kaxiras E, and Kim P 2019 *Nat. Mater.* **18** 448
- [19] Wagner G, Kwan Y H, Bultinck N, Simon S H, and Parameswaran S A 2022 *Phys. Rev. Lett.* **128** 156401
- [20] Pantaleón P A, Low T, and Guinea F 2021 *Phys. Rev. B* **103** 205403
- [21] de Jong T A, Benschop T, Chen X, Krasovskii E E, de Dood M J A, Tromp R M, Allan M P, and van der Molen S J 2022 *Nat. Commun.* **13** 70
- [22] Nakatsuji N, and Koshino M 2022 *Phys. Rev. B* **105** 245408
- [23] Kwan Y H, Wagner G, Soejima T, Zaletel M P, Simon S H, Parameswaran S A, and Bultinck N 2021 *Phys. Rev. X* **11** 041063
- [24] Kapfer M, Jessen B S, Eisele M E, Fu M, Danielsen D R, Darlington T P, Moore S L, Finney N R, Marchese A, Hsieh V, Majchrzak P, Jiang Z, Biswas D, Dudin P, Avila J, Watanabe K, Taniguchi T, Ulstrup S, Bøggild P, Schuck P J, Basov D N, Hone J, and Dean C R 2023 *Science* **381** 677
- [25] Lau C N, Bockrath M W, Mak K F, and Zhang F 2022 *Nature* **602** 41
- [26] Xie Y, Pierce A T, Park J M, Parker D E, Khalaf E, Ledwith P, Cao Y, Lee S H, Chen S, Forrester P R, Watanabe K, Taniguchi T, Vishwanath A, Jarillo-Herrero P, and Yacoby A 2021 *Nature* **600** 439
- [27] Das I, Lu X B, Herzog-Arbeitman J, Song Z D, Watanabe K, Taniguchi T, Bernevig B A, and Efetov D K 2021 *Nat. Phys.* **17** 710
- [28] Saito Y, Ge J Y, Rademaker L, Watanabe K, Taniguchi T, Abanin D A, and Young A F 2021 *Nat. Phys.* **17** 478
- [29] Wu S, Zhang Z Y, Watanabe K, Taniguchi T, and Andrei E Y 2021 *Nat. Mater.* **20** 488
- [30] Wang L, Meric I, Huang P Y, Gao Q, Gao Y, Tran H, Taniguchi T, Watanabe K, Campos L M, Muller D A, Guo J, Kim P, Hone J, Shepard K L, and Dean C R 2013 *Science* **342** 614
- [31] Kim K, Yankowitz M, Fallahazad B, Kang S, Movva H C P, Huang S, Larentis S, Corbet C M, Taniguchi T, Watanabe K, Banerjee S K, LeRoy B J, and Tutuc E 2016 *Nano Lett.* **16** 1989
- [32] Barber M E, Ma E Y, and Shen Z X 2021 *Nat. Rev. Phys.* **4** 61
- [33] Ohlberg D A A, Tami D, Gadelha A C, Neto E G S, Santana F C, Miranda D, Avelino W, Watanabe K, Taniguchi T, Campos L C, Ramirez J C, do Rego C G, Jorio A, and Medeiros-Ribeiro G 2021 *Nat. Commun.* **12** 2980
- [34] Huang X, Chen L X, Tang S J, Jiang C X, Chen C, Wang H S, Shen Z X, Wang H, and Cui Y T 2021 *Nano Lett.* **21** 4292
- [35] Lee K, Utama M I B, Kahn S, Samudrala A, Leconte N, Yang B, Wang S, Watanabe K, Taniguchi T, Altoé M V P, Zhang G, Weber-Bargioni A, Crommie M, Ashby P D, Jung J, Wang F, and Zettl A 2020 *Sci. Adv.* **6** eabd1919
- [36] Dean C R, Wang L, Maher P, Forsythe C, Ghahari F, Gao Y, Katoch J, Ishigami M, Moon P, Koshino M, Taniguchi T, Watanabe K, Shepard K L, Hone J, and Kim P 2013 *Nature* **497** 598
- [37] Nuckolls K P, Oh M, Wong D, Lian B, Watanabe K, Taniguchi T, Bernevig B A, and Yazdani A 2020 *Nature* **588** 610